Journal of Materials Chemistry B

ROYAL SOCIETY OF CHEMISTRY

PAPER

View Article Online
View Journal | View Issue

Cite this: J. Mater. Chem. B, 2023, 11, 1288

3D printed reduced graphene oxide-GelMA hybrid hydrogel scaffolds for potential neuralized bone regeneration†

Xinwei Zhang,[ab] Hao Zhang,[ab] Yi Zhang,[ab] Huimin Huangfu,[ab] Yixin Yang,[ab] Qiuyue Qin,[ab] Yidi Zhang *[ab] and Yanmin Zhou*[ab]

Peripheral nerves participate in bone growth and repair by secreting neurotransmitters, and enable new bone to possess physiological bone-sensing capability. However, it is difficult to achieve synchronized nerve regeneration during the healing process of large bone defects at present. As a bioactive nanomaterial, reduced graphene oxide (rGO) can promote neuronal differentiation and myelination of Schwann cells (SCs), while enhancing the adhesion and osteogenic differentiation of bone marrow mesenchymal stem cells (BMSCs) through its strong non-covalent binding ability. In this study, 3D printing-based rGO/GelMA hydrogels with enhanced osteogenic and neurogenic dual differentiation were used to simultaneously load SCs and BMSCs. By changing the concentration of rGO(0.03%/0.05%/0.1%), the compressive strength, rheological properties and aperture of the hydrogel can be improved. *In vitro*, cell live/death staining, phalloidin staining and SEM showed that cells loaded on the hydrogel had a high survival rate (85%) and good adhesion ability. *In vivo*, we found that the rGO/GelMA hydrogel exhibited the same low inflammatory response compared to the pure-GelMA group and the cell-only group, but surrounded by collagen fibers. Meanwhile, the osteogenic and neural proteins in the rGO/GelMA group were found to be highly expressed in immunohistochemistry and immunofluorescence. In this study, a scaffold material containing double cells was used to promote synergistic regeneration of nerves and bone, providing a promising strategy for the preparation of personalized and functionalized biomimetic bone material.

Received 16th September 2022,
Accepted 4th January 2023

DOI: 10.1039/d2tb01979e

rsc.li/materials-b

1. Introduction

Bone tissue is a structurally complex part of the human body, and the nerves and blood vessels in the bone are widely distributed in the Haversian canal and the Volkmann canal of the cortical bone.[1–3] On the one hand, sensory and sympathetic nerves participate in the growth and repair of bones by secreting substances such as neurotransmitters and neuropeptides.[4,5] On the other hand, intraosseous nerves sense changes in bone by conducting mechanical or electrical signals to maintain their normal physiological activities.[6] Sensory denervation may lead to loss of trabecular bone, resulting in decreased bone strength and impairment of new bone formatio.[7,8] In addition, for the bone lacking bone sensing ability, due to the lack of accurate and timely conduction to external stimuli, pathological responses may occur (for example, it is difficult to perceive whether the tooth is subjected to traumatic stress after the loss of nerves in the alveolar bone).[9] Therefore, simultaneous repair of intraosseous nerves is critical for functional bone regeneration. However, there are few reports on the synergistic regeneration of bone and nerve with biomimetic bone scaffolds.[10,11]

Cell therapy is considered a strategy to replace, repair or enhance the biological function of damaged tissues or systems by autologous or allogeneic cells.[12–14] Among them, bone marrow mesenchymal stem cells (BMSCs) are stem cells with the self-proliferation ability and multi-directional differentiation potential extracted from bone marrow. They are often loaded by scaffold materials for bone tissue regeneration for the study of osteogenesis.[15,16] Schwann cells (SCs) decompose and phagocytose myelin debris from distal nerve segments during functional recovery of injured peripheral nerves and proliferate to form Büngner's ribbons, which in turn guide axon regeneration in proximal segments.[17,18] BMSCs and SCs can promote the differentiation of each other.[19] Previous studies

[a] Hospital of Stomatology, Jilin University, Changchun 130000, China. E-mail: zhangyidi@jlu.edu.cn, zhouym@jlu.edu.cn
[b] Jilin Provincial Key Laboratory of Tooth Development and Bone Remodeling, Jilin University, Changchun 130000, China

† Electronic supplementary information (ESI) available. See DOI: https://doi.org/10.1039/d2tb01979e

have shown that SCs co-cultured with BMSCs on osteogenic scaffolds exhibited better proliferative capacity and nerve growth factor (NGF), s100, TrkA and brain-derived neurotrophic factor(BDNF) expression.[1]

Graphene oxide (GO) is a nanomaterial with a large number of hydrophilic functional groups and a large surface area. Due to its excellent mechanical properties and topographic features, it has attracted extensive attention in cell engineering applications.[20,21] However, many studies have shown that GO may have cytotoxicity and low electrical conductivity to a certain extent, and toxicity is related to exposure time, dose, and surface chemistry.[22] Reduced graphene oxide (rGO) is obtained by reducing GO to remove part of the oxygen functional groups. Reduction of GO to rGO reduces water dispersibility, making rGO more safe, stable, and conductive than GO *in vivo*.[23] rGO is rich in π–π stacking, hydrogen bonding, and electrostatic binding. It enables cell adhesion by promoting fibronectin extracellular protein adsorption, while also regulating stem cell growth and migration.[24] Studies have also shown that the high conductivity of reduced graphene oxide can modulate neural cell mobility and differentiation under electrical stimulation (ES), which will be beneficial to support the growth of neuronal cells in neural tissue engineering.[25]

Here, we combined 3D printing technology to prepare an rGO composite hydrogel scaffold for loading SCs and BMSCs simultaneously for synergistic regeneration of bone and nerve. By changing the concentration of rGO, the compressive strength, rheological properties and porosity of the hydrogel can be well improved. The adhesion of two different stem cells on the 3D-printed hydrogel scaffolds was improved, and they were induced to differentiate into osteogenic and neurogenic cells. *In vivo*, the rGO hydrogel scaffolds achieved multicellular delivery and differentiation (Scheme 1). Scaffolding materials based on 3D printing technology can achieve rapid, precise and personalized applications. At the same time, the loading of various stem cells makes functionalized biomimetic bone materials provide a promising strategy.

2. Materials and methods

2.1. Preparation of materials

Methacrylate anhydride gelatin (GelMA, 10w/v, Sunp Biotech, China) and photoinitiator (LAP, 0.25%w/v, Sunp Biotech, China) were dissolved in PBS and fully dissolved at 50 °C. Then rGO (0.03 mg ml^{-1}, 0.05 mg ml^{-1}, 0.1 mg ml^{-1}, XF Nano, China) was added to the GelMA precursor solution. Cyclic magnetic stirring (30 min) and ultrasonic vibration (30 min) 3 times, and finally completely dissolved. Finally, four different concentrations of bioinks (10% GelMA, 0.03% rGO/GelMA,

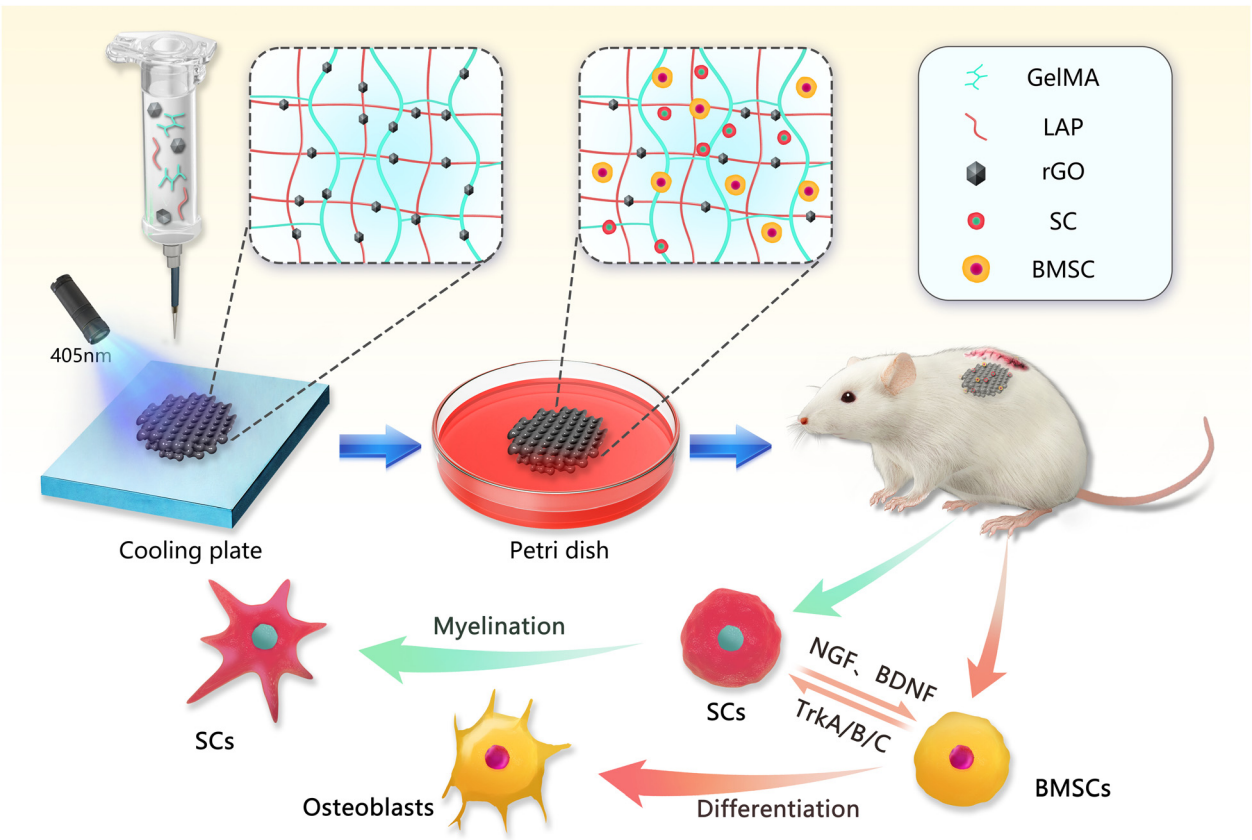

Scheme 1 Schematic diagram of the 3D bioprinting process of the rGO composite hydrogel scaffold, and the subcutaneous ectopic osteogenesis model in the rat *in vivo* experiment.

0.05% rGO/GelMA and 0.1% rGO/GelMA) were prepared as described above.

2.2. Scaffold fabrication

Before 3D printing, different concentrations of bioinks were transferred into cartridges. A bioprinter was used to make the scaffolds. The size of the scaffold is 15 × 15 × 1.6 mm. The temperature is 25 °C; the layer height is 0.2 mm; the line spacing is 1 mm; the printing speed is 3 $mm^3 s^{-1}$. The scaffolds were permanently cross-linked after 60 s cross-linking with 405 nm blue light on a cooling plate.

2.3. Material characterization

2.3.1. Scanning electron microscope (SEM) characterization. The scaffolds after complete cross-linking were vacuum freeze-dried for 24 h and gold sprayed. They were then placed under an SEM (FlexSEM 1000, Hitachi, Japan) field emission scanning electron microscope to observe their surfaces. We analyze the pore size by Image J software.

2.3.2. Mechanical property test. The precursor solution was completely photocured to form a cylinder with a height of 4 mm and a diameter of 10 mm. The samples were performed in a universal tester with a capacity of 100 N and a compression speed of 1 mm min^{-1}. The test was terminated when the specimen fractured. The compressive modulus is calculated from the slope of the strain–stress curve in the linear region (10–20% strain).

2.3.3. Testing of rheological properties. The viscosity and storage modulus of the hydrogels were tested using a rheometer (MCR 102e). The parameters are set to 25 °C, 1% constant variation and 10 rad s^{-1} constant angular frequency. The shear rate range of the viscosity test is 0.1–500 s^{-1}, the light source of 405 nm at a distance of 5 mm is selected for the photocrosslinking, and the temperature test is carried out at 10–40 °C. (n = 3)

2.3.4. Swelling test. The printed scaffolds were fully immersed in PBS. Samples were weighed from the hydrogels collected from PBS at each predetermined time interval, and excess liquid was removed with filter paper. The formula for calculating SR is:

$$SR = (W_t - W_0)/W_0 \times 100\%$$

W_0 and W_t are the initial weight and the swollen weight of the hydrogel, respectively. (n = 3)

2.3.5. Degradation assay. The scaffolds were completely immersed in PBS containing type II collagenase (Solarbio, China) (1.25 U ml^{-1}). Hydrogel samples were weighed every 2 days at 37 °C. The following is the calculation of the degradation rate:

$$\text{Degradation rate } (\%) = W_t/W_0 \times 100\%$$

W_t represents the weight of the remaining hydrogel at each time point, and W_0 represents the initial weight of the hydrogel (n = 3).

2.4. *In vitro* cytocompatibility

2.4.1. Cell culture. Primary rat BMSCs were isolated by harvesting bone marrow from the femur and tibia of young male SD rats (5–7 days) according to previously published protocols. rBMSCs were used between passages 3 and 5. Rat Schwann 96 cells were obtained from Guangzhou Saiku Biotechnology Co., Ltd. (China). After sterilization, the scaffolds were placed in 24-well culture plates. The rBMSCs and SCs between passages 3 and 5 were trypsinized, centrifuged, resuspended, and seeded on the surface of the scaffold at 5 × 10^4 cells per well.

2.4.2. Cell viability assay. On the 1st, 4th and 7th days after the cells were incubated, they were stained according to the instructions of the Living/Death Staining Kit (Solarbio, China). The image was taken by laser confocal microscope. It is used to evaluate the viability of cells on the scaffold surface.

2.4.3. Cell proliferation assay. Cell Counting Kit-8 (CCK-8, NCM Biotech Co., Ltd, China) was used to detect cell proliferation. On days 1, 4, and 7 of cell seeding, optical density (OD) values were measured at 450 nm using a microplate reader after incubation for 1 hour using the cck-8 kit.

2.4.4. Hemolysis test. Fresh anticoagulated SD rat blood was diluted with 0.9% NaCl solution at a volume ratio of 4 : 5, and the stents of different concentrations in each group were immersed in 10 ml of physiological saline for 24 h. Then add 0.2 ml of diluted blood to each group of normal saline, shake gently, and let stand at 37 °C for 60 min. After centrifugation at 1000 rpm for 5 min, the absorbance of the supernatant was measured at 545 nm. The hemolysis rate is calculated as follows:

$$\text{Hemolysis rate } (\%) = (D_t - D_{nc})/(D_{pc} - D_{nc}) \times 100\%$$

where D_t is the absorbance of the sample, D_{nc} is the absorbance of the saline group(negative), and D_{pc} is the absorbance of the distilled water group(positive).

2.4.5. Cell adhesion assay. The morphological changes of cells on the surface of scaffolds at day 1 and day 7 after cell seeding were observed by phalloidin/DAPI (Solarbio, China) staining. Cells were fixed with 4% paraformaldehyde for 15 min. Cells were imaged by confocal laser scanning microscopy after 30 min of phalloidin staining (red fluorescence) and 3 min of DAPI counterstaining (blue fluorescence).

Scanning electron microscopy was also used to directly observe the morphology of cells on the scaffold surface. The cells seeded for 48 h were soaked in electron microscope fixative solution at 4 °C overnight. Then, the samples were dehydrated step by step with different concentrations of ethanol (30%, 40%, 50%, 60%, 70%, 80%, 90%, 95%, 100% for 10 minutes each) and then sprayed with gold for SEM detection.

2.5. *In vitro* osteogenic and neurogenic differentiation

2.5.1. Determination of alkaline phosphatase activity. BMSCs at passages 3–5 were seeded in 12-well plates at a density of 2 × 10^4 cells per well. The cells were co-cultured with GelMA scaffold and rGO/GelMA scaffold, and the simple

cell group without scaffold was the control group. In osteogenic induction medium [α-MEM medium containing 10% fetal bovine serum (FBS, Hyclone, Logan, UT), 10 mM β-glycerophosphate (Sigma-Aldrich, St Louis, MO), 50 μg ml^{-1} ascorbic acid (Sigma-Aldrich, St Louis, MO), 1% penicillin/streptomycin (P/S, Hyclone, Logan, UT) and 10 nM dexamethasone (Sigma-Aldrich, St Louis, MO)] on the 7th and 14th days after culture, by BCIP/NBT alkaline phosphatase chromogenic kit (Beyotime, Shanghai, China) evaluate the expression of ALP. Briefly, cells were fixed with 4% paraformaldehyde for 15 min, washed with PBS, and incubated with ALP staining for 30 min in the dark. Finally imaged with a scanner. Following the same protocol, the activity of ALP was determined using an alkaline phosphatase assay kit (Beyotime, Shanghai, China).

2.5.2. Alizarin red staining (ARS). BMSCs and scaffolds were co-cultured according to the protocol described above. On days 21 and 28 after osteogenic induction, ARS solution (Cyagen, Suzhou, China) was used to detect calcium nodules during osteogenic differentiation. After staining was completed, it was imaged with a scanner. Chlorohexadecylpyridine (RHAWN, Shanghai, China) was used to dissolve alizarin red calcium nodules and absorbance at 562 nm for further quantitative analysis.

2.5.3. Quantitative real-time polymerase chain reaction (qRT-PCR). The scaffolds loaded with day 14 BMSCs and SCs were immersed in RNAiso Plus (Takara, Japan), respectively, for total mRNA extraction. RNA reverse transcription and cDNA amplification were performed according to the instructions of the kit. It was used to assess Schwann cell myelination genes [nerve growth factor (NGF), neuronal cell adhesion molecule (NCAM), early growth response-2 (Krox20) and peripheral myelin protein-22 (PMP22)] and Expression of bone-related markers [collagen type I (COL1), Runt-related transcription factor-2 (RUNX2), alkaline phosphatase (ALP), and osteocalcin (OCN)]. (Table S1, ESI†)

2.6. *In vivo* experiments – subcutaneous heterotopic transplantation in rats

To evaluate the viability and function of the transplanted cells and the biological properties of the biomaterials, ectopic subcutaneous implantation was performed using a hydrogel scaffold loaded with two types of cells (rBMSCs and SCs). All experimental animal procedures were approved by Jilin University according to international standards for animal welfare (authorization number: KT202003217). Twenty SD rats (male, 12 weeks old, with an average weight about of 250 g) were randomly divided into 5 groups, including group I (BMSCs/SCs), group II (GelMA), group III (rGO/GelMA), group IV (Cell-loaded GelMA) and group V (Cell-loaded rGO/GelMA) (4 each). Cells were seeded on scaffolds and cultured for 7 days before surgery. Surgery is performed under anesthesia in a sterile environment. A 1.5 cm incision was made in the dorsal skin with a scalpel, the subcutaneous tissue was separated, and the hydrogel scaffold was transplanted under the skin and sutured tightly. At week 8 post-transplantation, whole regenerated tissue specimens were removed and fixed in 10% formalin. Specimens were dehydrated in graded ethanol and embedded in paraffin. Excised from the center of the regeneration site and stained with hematoxylin and eosin (H&E), Masson staining, immunohistochemical staining (s100β and OCN) and immunofluorescence (CD31, NGF, Runx2 and Col-1) according to standard protocols. All tissue sections were observed and analyzed under a light microscope/confocal microscope. The degree of inflammatory/positive cells in implant tissue sections *in vivo* were evaluated and observed under 5 areas with 1000 μm^2 were selected from 3 replicate slides randomly, examined, and photographed through a light microscope/confocal microscope at 200 × magnification for the inflammatory/positive areas, and 400 × magnification to count the immune/positive cells.

2.6.1. Hematoxylin-eosin staining. Stain cell nuclei (3 min with hematoxylin; 1% hydrochloric acid alcohol differentiation for a few seconds; 0.6% ammonia water for a few seconds), stain cytoplasm (dye with eosin for 1 min), dehydrate the slide (95% alcohol I 5 min; 95% alcohol II 5 min; anhydrous Ethanol I 5 min; absolute ethanol II 5 min; xylene I 5 min; xylene II 5 min dehydrated and transparent; neutral gum for sealing).

The degree of inflammatory cells in implant tissue sections and animal internal organs (heart, liver, spleen, lung and kidney) and the metabolism of graphene *in vivo* were evaluated and observed by H&E staining.

Masson staining. Cell nuclei stained with hematoxylin (3 min), ponceau red stained (5 min), phosphomolybdic acid treated (3 min), aniline blue stained (1 min), differentiated (1% glacial acetic acid for 1 min), dehydrated and mounted, and examined for new collagen fibers under a microscope.

Immunofluorescence (CD31, NGF, Runx2 and Col-1): Antigen retrieval (adding to 0.01 M citrate buffer and repairing by heating), permeabilization with 0.5% Triton X-100 at room temperature for 20 min), blocking (blocking with 2% BSA for 30 min), incubation with primary antibody (overnight at 4 °C)), incubated with secondary antibody (2 h at room temperature), stained cell nuclei (30 s at room temperature with DAPI), and mounted (anti-fade glycerol). The distribution and number of positive cells (red fluorescence/green fluorescence) were observed under confocal laser microscopy.

Immunohistochemistry (s100β and OCN). Antigen retrieval, blocking (incubate with 3% hydrogen peroxide at room temperature for 15 minutes), localization (determination of staining range with immunohistochemical pen), incubate primary antibody (overnight at 4 °C), incubate secondary antibody (incubate for 1 hour after rewarming at room temperature), color development (DAB chromogenic solution, stop staining after observing under the microscope until the color is suitable), hematoxylin counterstaining (3 min), dehydration and sealing. The distribution and number of positive cells (dark brown) were observed under a microscope.

2.7. Statistical analysis

Statistical analysis was performed using Prism 8.0. Data are presented as mean ± standard deviation. Each group of

samples was repeated three times. A *t*-test or one-/two-way ANOVA was performed to determine statistical significance. A *p*-value less than 0.05 was considered statistically significant.

3. Results and discussion

3.1. Physical properties of bioinks and 3D printed scaffolds

According to previous reports, reduced graphene oxide with hydrophobic properties is difficult to dissolve in an aqueous phase. However, rGO in GelMA precursor solution can be completely dissolved under ultrasonic vibration and magnetic stirring.[26] With increasing rGO concentration in the hydrogel system (0.03%, 0.05% and 0.1%), the color of the composite hydrogel gradually deepened (Fig. 1A). The morphology of the lyophilized scaffolds were observed by SEM (Fig. 1B). All scaffolds have a regular grid structure, and the grid space is about 1 mm, which corresponds to the parameters set by 3D printing. Interestingly, we found that with the addition of rGO, the pore size of the scaffolds decreased significantly (GelMA 68.51 ± 17.50 μm; 0.03%rGO/GelMA 39.48 ± 9.95 μm;

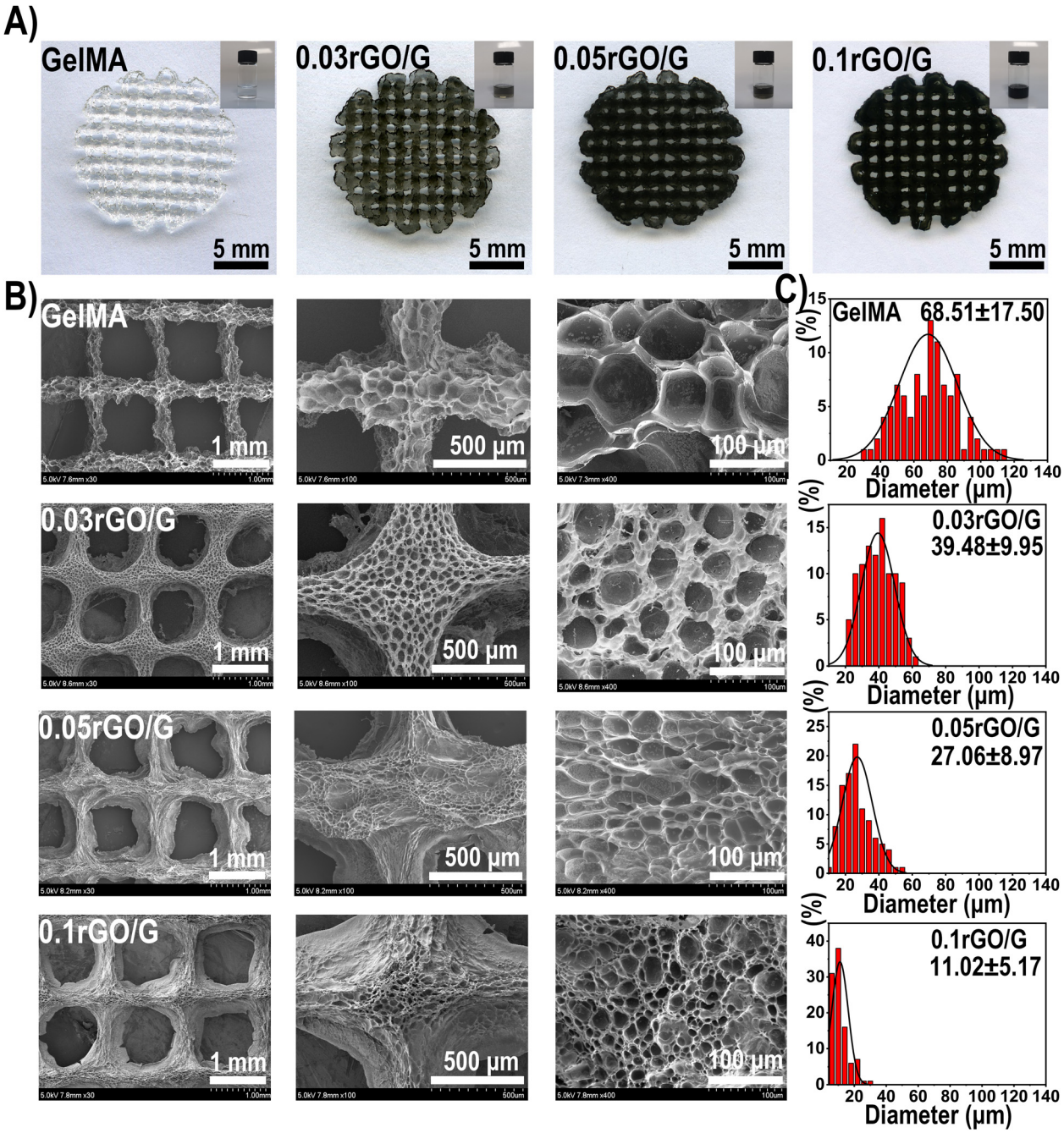

Fig. 1 (A) Macroscopic images of GelMA precursor solutions and 3D scaffolds with different rGO concentrations. (B) Scanning electron microscope image of the rGO composite hydrogel scaffold. (C) Quantitative analysis of the pore size of the hydrogel.

0.05%rGO/GelMA 27.06 ± 8.97 μm; 0.1%rGO/GelMA 11.02 ± 5.17 μm) (Fig. 1C). The reason for the smaller pore size of the scaffold may be that the graphene nanosheets increase the density of crosslinks inside the gel.

In the testing of mechanical properties, we found that the compressive strength of 0.03%rGO/GelMA group and 0.05%rGO/GelMA group (GelMA 90.52 kPa; 0.03%rGO/GelMA 125.90 kPa; 0.05%rGO/GelMA 174.26 kPa; 0.1%rGO/GelMA 51.01 kPa) and ultimate strain (GelMA 63.33%; 0.03%rGO/GelMA 73.33%; 0.05%rGO/GelMA 79.17%; 0.1%rGO/GelMA 70.67%) were significantly better (Fig. 2A–D) (Table S2, ESI†). Interestingly, we observed lower mechanical properties in the

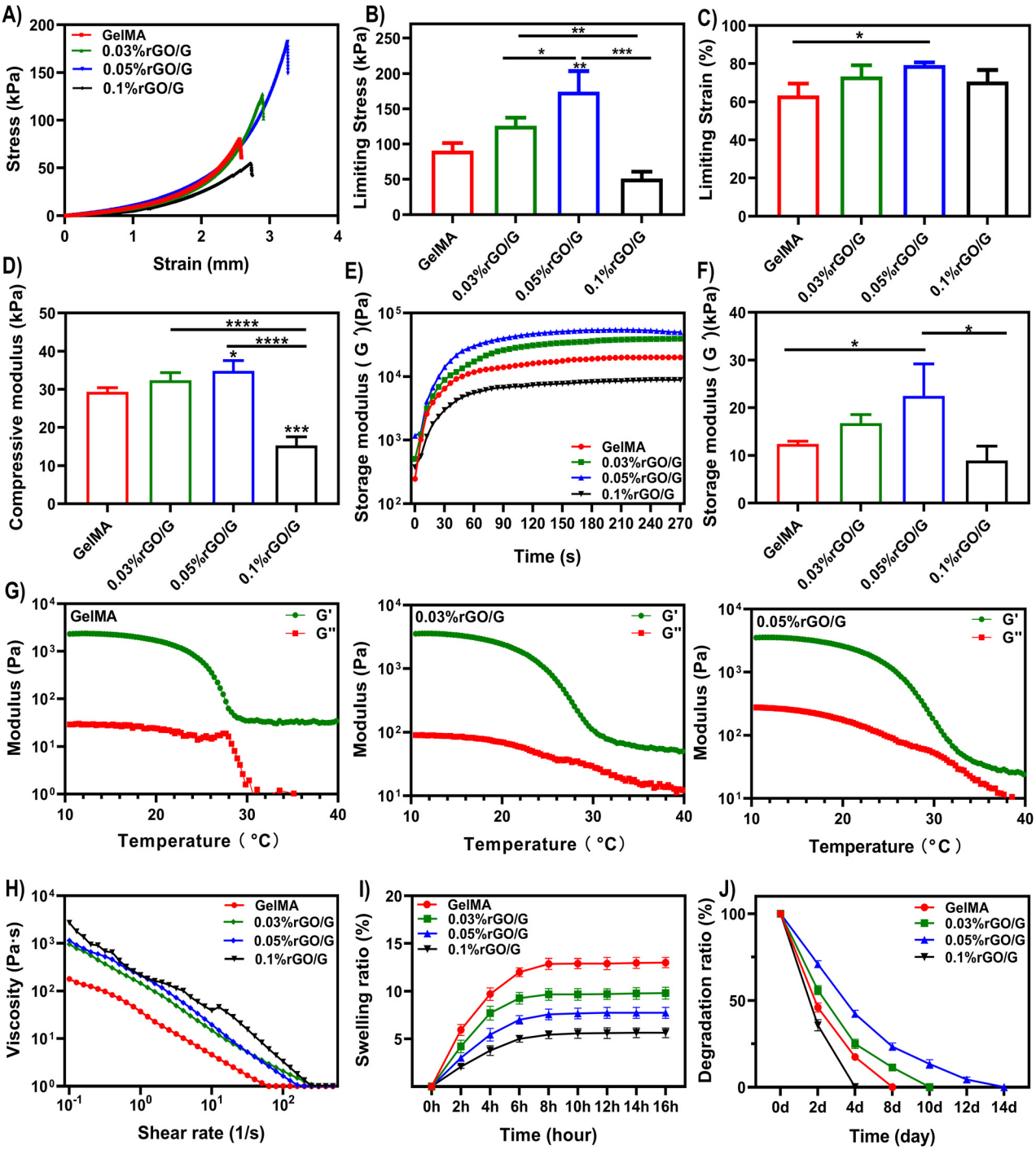

Fig. 2 Stress–strain curve (A), ultimate stress (B), ultimate strain (C) and compressive modulus (strain: 10–20%) (D) at room temperature. (E) Storage under 405 nm illumination Modulus G' change and storage modulus (F) at 60 s. (G) Temperature-storage modulus G'/loss modulus G'' plot. (H) Relationship between shear rate and viscosity. (I) Swelling properties (J) degradation rate. $p < 0.05$ indicates significant difference ($n = 3$, $^{*}p < 0.05$, $^{**}p < 0.01$, $^{***}p < 0.001$, $^{****}p < 0.0001$, *ns* = no significance).

0.1%rGO/GelMA group instead. As the concentration of rGO increases, due to its strong light-shielding ability, it is difficult to achieve complete photo-crosslinking in the interior of the hydrogel, resulting in insufficient mechanical properties.[26] The effect of photocuring time on the storage modulus of the hydrogel was further explored. We found that the storage modulus of the hydrogels in the rGO/GelMA group (0.03%rGO 39.69 kPa; 0.05%rGO 54.84 kPa) was significantly higher than that of the pure GelMA group (20.11 kPa) after 405 nm light curing for 60 s (Fig. 2E and F) (Table S3, ESI†). Notably, a high concentration of rGO resulted in a decrease in the storage modulus (0.05%rGO: 88.88 kPa) of the hydrogel, which was even much lower than that of the pure GelMA group. This is consistent with the previous compression test results.

Rheology describes the deformation and flow properties of materials under the influence of external forces. And it is the physicochemical parameter that has the greatest impact on the printability of hydrogels.[27] In extrusion printing, the shear-thinning properties simplify printing and affect the initial shape of the bioscaffold, and the viscosity decreases during the extrusion phase, where the shear force increases significantly. After extrusion, the shear rate decreases and the viscosity increases accordingly, helping to maintain the original shape of the print.[28] The rGO/GelMA composite bioink showed higher viscosity than other curves (5974.09 Pa·s) at the low shear rate, while at a high shear rate, the viscosity rapidly decreased to almost the same level as the other curves (0.12 Pa·s) (Fig. 2H). All groups of bioinks have excellent shear thinning properties. Due to the shear-thinning behavior, all concentrations of rGO hydrogels can pass through the 0.2 mm printer needle and 3D print smoothly. In addition to good shear thinning properties and suitable viscosity, an ideal printable bioink should also have excellent temperature sensitivity.[29,30] In our results, the storage moduli (G') of all inks at low temperature were much larger than the loss moduli (G'') (Fig. 2G). For freshly printed scaffolds, temporary physical cross-linking at low temperature is crucial to maintain the accuracy of the printed morphology.[31] The swelling properties of hydrogels have a significant impact on maintaining the initial shape and mechanical stability of 3D printed structures. Excessive swelling ratios may cause the structure to swell and become brittle.[32] The results show that with the increase of the concentration, the swelling ratio is greatly reduced, and the rGO-added scaffold retains the original morphology to the greatest extent (Fig. 2I). The rapid degradation of hydrogels used in bone tissue engineering has always been a difficulty worth improving.[33,34] Relevant literature indicates that the uncontrolled release of loaded bioactive growth factors and stem cells is directly related to the rapid degradation of hydrogels. This is difficult to match with a bone repair time of more than 3 months.[35] Collagenase type II [matrix metalloproteinase 8 (MMP-8)] is the major proteolytic enzyme involved in bone wound healing.[36] GelMA is enzymatically degraded, as gelatin contains sequences that are recognized by collagenases.[37] To assess degradation, the hydrogels were immersed in collagenase type II solution (1.25 U ml^{-1}). Except for 0.1%rGO/GelMA, which could not be fully photocrosslinked, the degradation rate of other groups was significantly lower than that of the GelMA group due to changes in pore structure and scaffold cross-linking density (Fig. 2J). In summary, during the preparation process of 3D printing, we found that the hydrogel precursor was easier to pass through the 0.2 mm nozzle smoothly, as the concentration of rGO increased. In rheological experiments, hydrogels containing 0.05% and 0.1% rGO/GelMA performed better than the control group. Considering the physical properties and the differentiation potential of cells, we chose a concentration of 0.05% rGO/GelMA as the experimental group for our subsequent *in vivo* and *in vitro* experiments.

3.2. *In vitro* cytocompatibility

Stem cells are expected to be effectively utilized in damaged tissues because of their dual potentials of proliferation and differentiation. But how to achieve long-term survival and retention of transplanted stem cells is a big problem.[38,39] To study the cell viability of rBMSCs in the 3D printed scaffolds, live (green)/dead (red) staining was performed in culture medium for 1 day, 4 days and 7 days, respectively. On the 7th day, the proportion of living cells in each group was more than 85%. At the same time, the fluorescence intensity of SCs and BMSCs loaded in rGO/GelMA is higher than that of the GelMA group. It is worth noting that the live/dead staining already showed a similar trend on day 1 (Fig. 3A, C). The resulting analysis of CCK-8 detection showed a similar tendency to that of live/dead staining (Fig. 3B), suggesting that the rGO in the scaffolds promotes cell proliferation. These results indicate that the addition of rGO improves the cell adhesion ability of the hydrogel.[40] Further the morphology of BMSCs and SCs on the scaffold was detected by cytoskeletal protein F-actin (red)/DAPI (blue) staining at 1 and 7 days. To our surprise, BMSCs on the rGO/GelMA exhibited a more stretched shape compared with the G group in the early stage (day 1), which indicates the excellent cytocompatibility of rGO in the scaffold. A more prominent tendency with the larger spreading area (Fig. 3D and E) and faster proliferation rate (Fig. 3B) was shown in the rGO/GelMA group for both BMSCs and SCs. We further observed the morphology of the cells by SEM after cell seeding for 48 hours, both SC and BMSCs exhibit a smooth cell membrane, and the cell on the rGO/GelMA spread better compared with the GelMA group (Fig. 3F). According to previous reports, rGO hydrogels with electrical conductivity can support cell viscosity and migration by mediating cell bioelectricity signals.[41] At the same time, our results show that after the addition of rGO, hydrogels have improved cell proliferation and cell adhesion. The reason is that rGO retains some oxygen-containing groups that can adhere to serum proteins and endow the scaffold with better cell attachment ability.[42] Promoting the adhesion of stem cells by changing the surface morphology or functional groups of biomaterials is a common method for stem cell transplantation. For example the RGD sequence consisting of arginine, glycine and aspartic acid mediates cell attachment *via* fibronectin.[43] Although RGD can improve the adhesion, it is easy to disappear in the

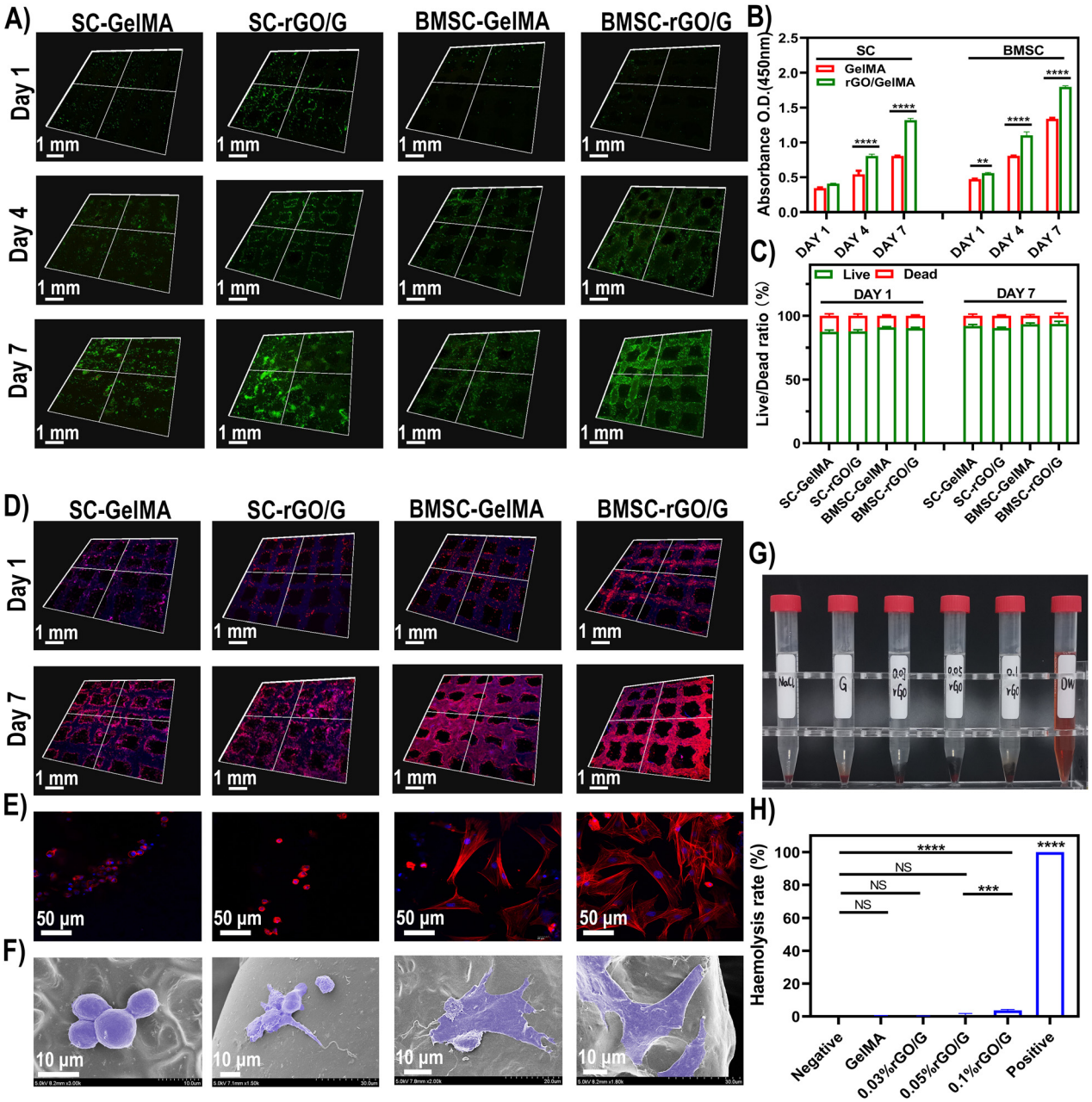

Fig. 3 (A) Live (green)/dead (red) staining of cells at 1, 4 and 7 days after cell seeding. (B) CCK-8 assay. (C) Quantitative analysis of live-dead staining assay. (D and E) 3D images of the morphology of BMSCs and SCs on the scaffold surface by cytoskeletal protein F-actin (red)/DAPI (blue) staining at 1 and 7 days. (F) Scanning electron micrograph of seeded cells at 48 hours. Actual pictures (G) and absorbance (H) of hemolysis experiments of different rGO concentrations of hydrogels. $p < 0.05$ indicates significant difference ($n = 3$, *$p < 0.05$, **$p < 0.01$, ***$p < 0.001$, ****$p < 0.0001$, *ns* = no significance).

physiological environment. The controlled release design can alleviate its rapid dissolution in the surrounding environment.[44] Polydopamine (PDA) can also improve cell adhesion in tissue engineering. PDA contains many hydrophilic functional groups, such as hydrophilic amino groups and hydroxyl groups, which can provide hydrophilic groups on the hydrophobic surface, thereby improving the hydrophilicity of the surface of biomaterials, thereby enhancing the ability of cell adhesion.[45] Natural polymers such as silk fibroin with better biocompatibility are also commonly used to improve cell migration and adhesion.[46] As a carbon allotrope, reduced graphene oxide has a two-dimensional and honeycomb structure with strong π bonds and large surface area. Based on the above structure, rGO can improve the cell adhesion and conductivity of the material surface. Among them, the conductivity is closely related to the number of layers of graphene. In fact, conductive materials usually rely on external stimuli from the environment to improve the growth, attachment, and differentiation of nerve cells. And the three-dimensional preparation of graphene nanocomposite

channels can also significantly up-regulate the biological activity of neural stem cells.[47]

Additionally, hemocompatibility testing was performed to test the effects of different scaffolds on red blood cells (RBCs), platelets, thrombosis, and coagulation, to determine whether the biomaterial is suitable for animal studies or clinical trials.[48] Through the hemolysis experiment, the hemolysis rate slightly increased with the increase of rGO concentration (Fig. 3G and H). However, according to the standard hemolytic index [ASTM F756-00(2000)], all groups of materials can be defined as non-hemolytic (<2%).

3.3. *In vitro* osteogenic and neurogenic differentiation

Bone scaffolds contact directly with the cells and provide the extracellular matrix (ECM) for cell adhesion, proliferation, and differentiation.[49–51] rGO has been reported to increase the stability of adsorbed proteins, such as bone morphogenetic protein 2 (BMP-2), and eventually improve cell adhesion, proliferation, and osteogenic differentiation.[52] The osteoblast phenotype is specifically obtained in two stages. In the first stage, the cells proliferate and the matrix matures. During 10–15 days of cell proliferation and matrix maturation, specific proteins associated with the osteocyte phenotype, such as ALP, can be detected. In the second stage of osteoblastic phenotype acquisition, matrix mineralization, the production of late bone markers and the production of calcium nodules after up to 25–30 days.[53] To investigate the osteogenic differentiation ability of rGO decorated GelMA scaffolds, the ALP activity and calcium deposition were tested. In our results, ALP staining was darker on days 7 and 14 in the rGO/GelMA group compared to the control and GelMA groups, representing high expression in the osteogenic direction. Notably, there was no difference in ALP staining between the GelMA group and the control group (Fig. 4A). In the activity experiment of ALP, the absorbance of the rGO group was also significantly higher than that of the other two groups on day 7 and 14 (Fig. 4B). BMSCs in each group formed orange-red calcium nodules on the 21st and 28th day. Calcium nodules in the rGO/GelMA group produced more calcium nodules compared to the control and pure GelMA groups (Fig. 4C). Chlorohexadecylpyridine was used to dissolve calcium nodules for further quantitative analysis (Fig. 4D). To further explore the osteogenic differentiation ability, we detected the relative mRNA expression levels of RUNX2, ALP, Col-1 and OCN by qRT-PCR at the gene level. The expression of osteogenesis-related genes was significantly enhanced in the rGO/GelMA group after 14 days of osteogenic induction (Fig. 4E). As far as we know, graphene derivatives have adsorption effects on dexamethasone and β-glycerophosphate.[54] As a member of glucocorticoid, Dex can participate in the expression of some signal molecules in the process of osteogenesis.[55] Osteoblasts cultured on graphene exhibited higher levels of mineralization and significantly upregulated osteogenic genes and proteins, including Runx2, Col-1 and OCN.[56]

Myelination of SC is a prerequisite during nerve regeneration.[57] Among them, neuronal cell adhesion molecule (NCAM) is an indicator of SCs myelination. It is only expressed in immature SCs and is reduced in myelination of SCs. In contrast, the expression levels of NGF, PMP22, and Krox20 were increased in myelinated SCs.[58] As shown in Fig. 4F, NCAM gene expression was significantly decreased on rGO/GelMA scaffolds compared to GelMA scaffolds, while NGF, PMP22 and Krox20 gene expression levels were significantly increased ($p < 0.05$). The results indicated that the presence of rGO promoted SCs myelination.

3.4. *In vivo* experiments – subcutaneous heterotopic transplantation in rats

At present, ideal bone inducing materials loaded with stem cells should have three key characteristics, including successful transplantation; promote differentiation and heterotopic osteogenesis.[59] To evaluate the viability and function of transplanted cells and the biological characteristics of biomaterials, scaffolds loaded with two types of cells (BMSCs and SCs) were transplanted ectopically subcutaneously (Fig. S1, ESI†). According to previous research reports, BMSCs co-cultured with SCs showed higher proliferation ability and osteogenic differentiation potential. Its related mechanism of action is mainly realized through the interaction between NGF, BDNF, TrkA, S100 and other cell signaling molecules.[1] As shown, the *in vivo* experiments were divided into 5 groups (Fig. 5A). In group I, the groups in which cells were directly injected into the subcutaneous tissue (BMSCs and SCs groups) did not show new bone and fewer blood vessel formation due to low cell retention. For the material-only groups (GelMA and rGO/GelMA), the scaffolds resulted in the formation of an ordered arrangement of tissues without obvious inflammatory response, confirming the excellent biocompatibility of GelMA and rGO (Fig. S2, ESI†). Compared with the scaffold group not loaded with cells, the scaffolds loaded with BMSCs and SCs were surrounded by a large number of collagen fibers, which were stained blue under Masson staining indicating the excellent osteogenic ability of the scaffolds (Fig. 5B). Collagen fibers (97%) are the most abundant protein in the bone extracellular matrix. In the process of osteogenesis, hydroxyapatite crystals are mainly arranged in a periodic and staggered manner along collagen fibers, thereby realizing bone repair and regeneration.[60] Then we further used immunofluorescence(IF) staining to observe the trend or situation of ectopic bone formation *in vivo*. The key to determining the biomaterial for stem cell transplantation is the survival rate and osteogenic differentiation of the transplanted cells. When the biomaterial is transplanted into the body, the stem cells can successfully complete the proliferation and differentiation into osteoblasts. During this period, osteoinductive materials serve space for the growth of BMSCs, absorb endogenous growth factors, and promote the proliferation and osteogenic differentiation of MSCs.[61] Here, immunofluorescence staining showed that 8 weeks after implantation in the Cell-rGO/GelMA group, the transplanted stem cells clearly expressed NGF, Runx2 and Col-1 (markers of osteoblasts/Schwann cells) in the implanted area (Fig. 6). At the same time, the vascularized CD31 molecule also showed high expression(Fig. S3, ESI†). The lower concentration of rGO can

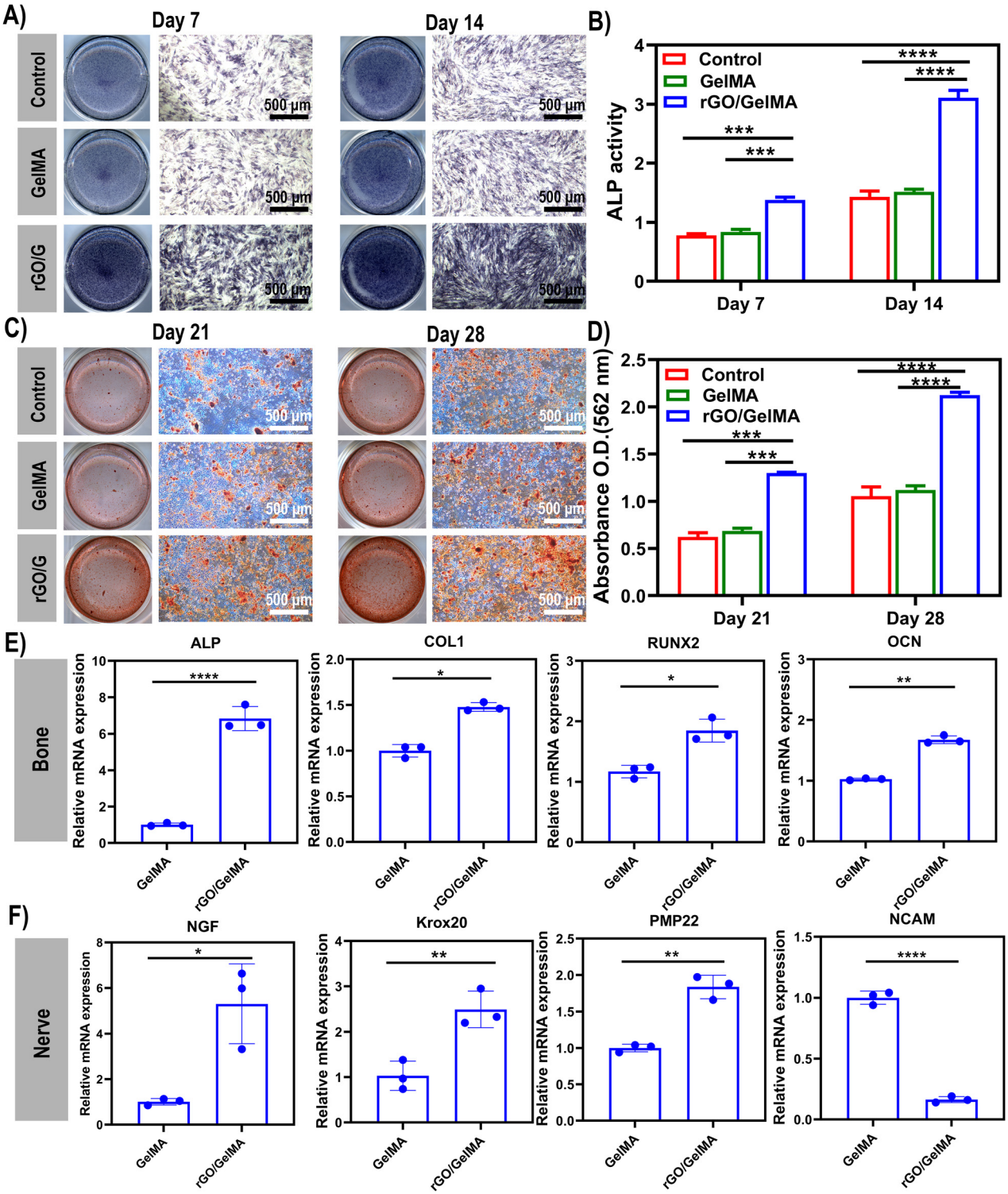

Fig. 4 (A and B) Alkaline phosphatase (ALP) staining and ALP activity of bone marrow mesenchymal stem cells co-cultured with SCs. (C and D) Alizarin red staining (ARS) and quantitative analysis of each group on the 21st and 28th days. (E) The osteogenesis related genes (RUNX2, ALP, COL-1 and OCN) of BMSC on the 14th day were determined by quantitative real-time polymerase chain reaction (qRT-PCR). (F) The myelination related genes (NCAM, NGF, PMP22 and Krox20) of Schwann cells cultured for 14 days were determined by qRT-PCR. $p < 0.05$ indicates significant difference ($n = 3$, *$p < 0.05$, **$p < 0.01$, ***$p < 0.001$, ***$p < 0.001$, *ns* = no significant difference).

enhance the migration of endothelial cells and show the characteristics of promoting angiogenesis.[62] New blood vessels form into regenerated peripheral nerves to provide nutritional support. Meanwhile, graphene oxide derivatives have also been shown to accelerate osteogenic differentiation by enhancing the expression of nestin, β-tubulin III and MAP2 to promote

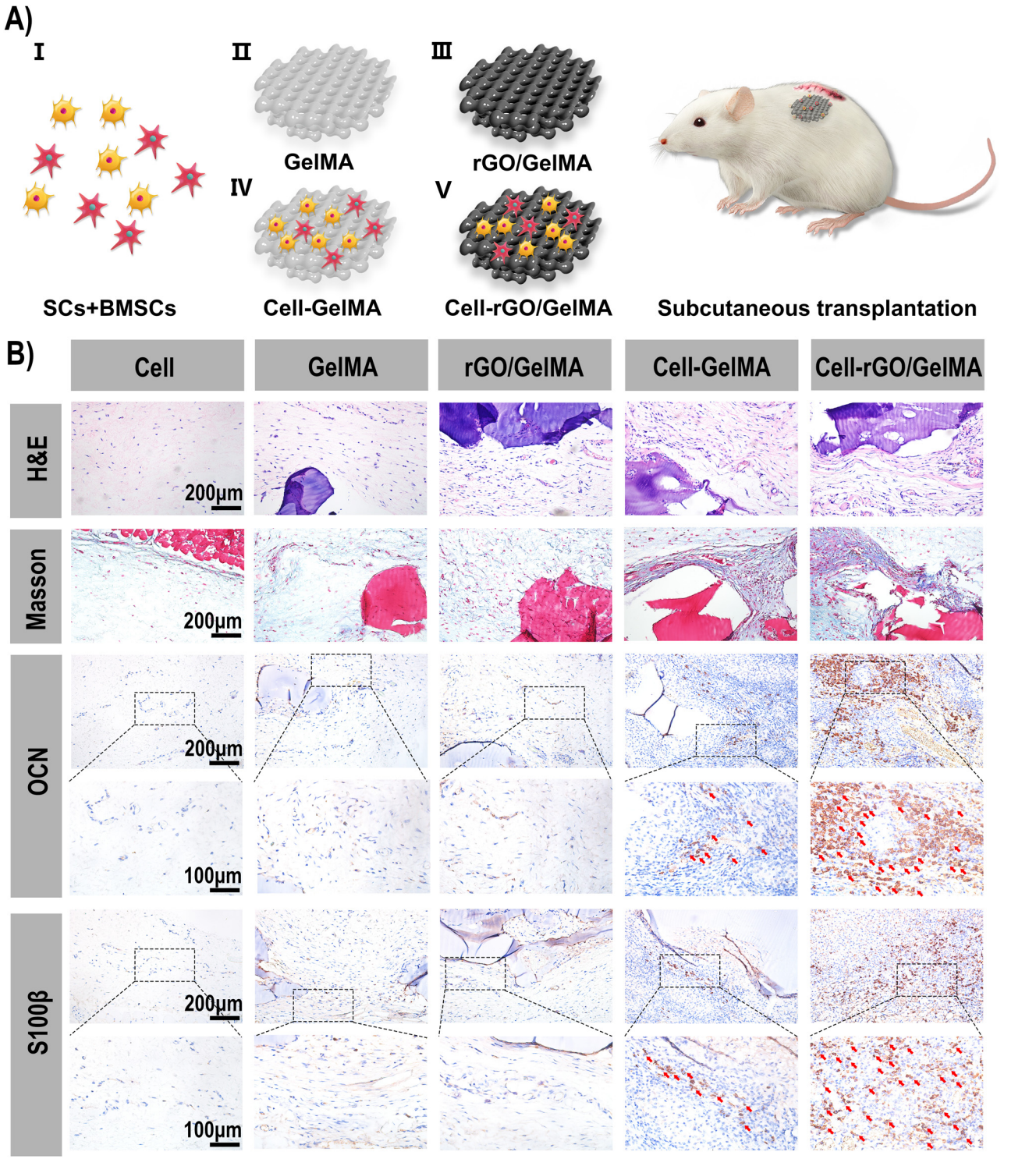

Fig. 5 (A) Schematic diagram of the *in vivo* experiments [Group I (BMSCs/SCs), Group II (GelMA), Group III (rGO/GelMA), Group IV (cell-loaded GelMA), and Group V (cell-loaded rGO/GelMA)]. (B) H&E, Masson staining and Immunohistochemical staining (OCN and S100β) (positive cells are indicated by red arrows) of tissue sections after 8 weeks of *in vivo* experiments.

neuronal differentiation, adhesion, and proliferation. Activation of the mechanosensitive integrin-FAK axis also plays an important role in osteogenic induction.[63] Immunohistochemical staining was performed to further assess neuralized bone formation (Fig. 5B). The expression of S100β and OCN was weaker in the cell-only group and the material-only group. In contrast, strong expression of OCN was found in the BMSCs and SCs-loaded scaffold groups, which was attributed to the

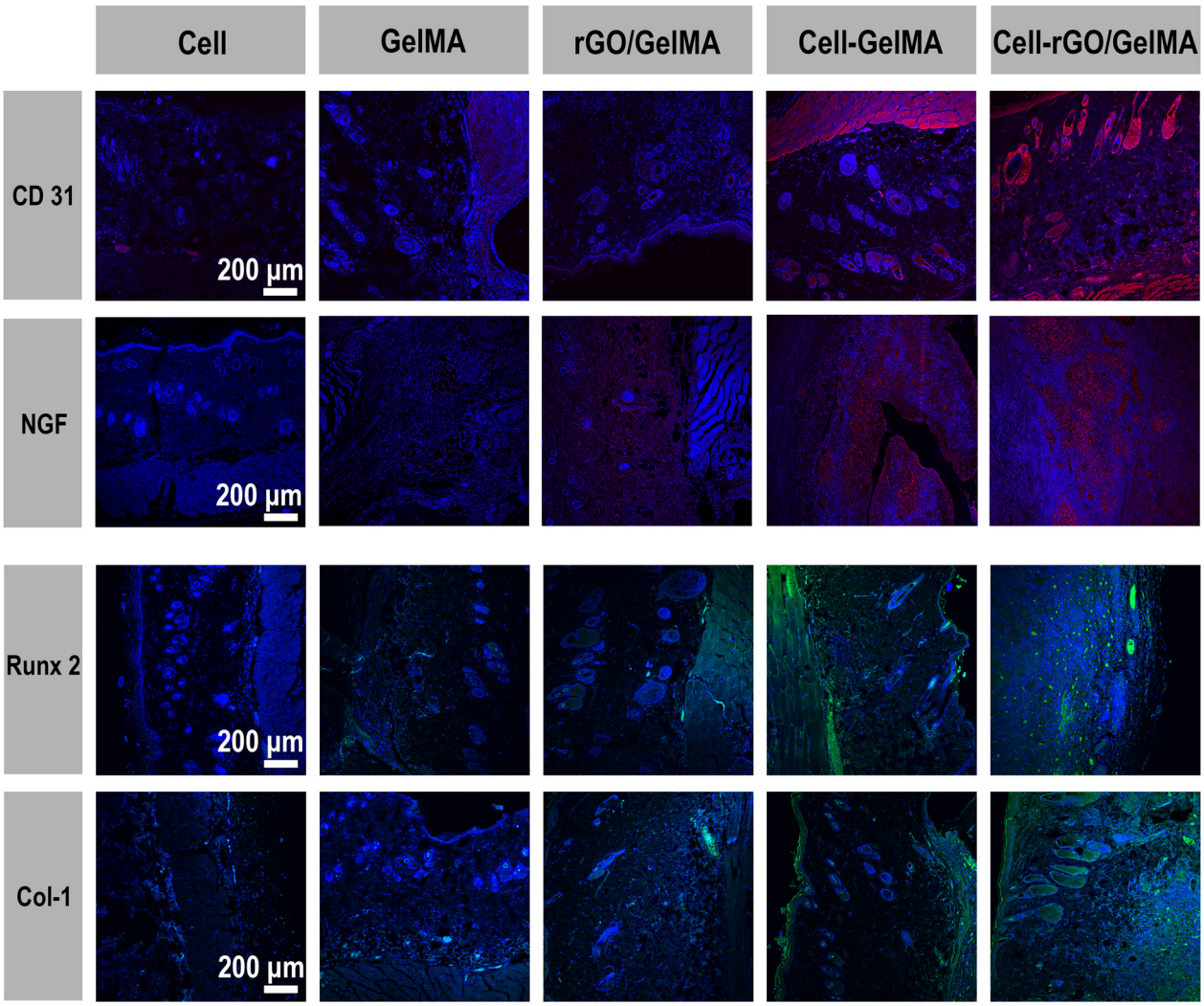

Fig. 6 Immunofluorescence staining of tissue sections (CD31, NGF, Runx2 and Col-1) after 8 weeks of *in vivo* experiments.

transplanted BMSCs. At the same time, s100β was also highly expressed, which was attributed to the transplanted SCs. The synergy of BMSCs and SCs is thought to make a significant contribution to regenerating neuralized osteoid tissue. Overall, the rGO-added hydrogel scaffolds showed good cell adhesion compared to the pure GelMA scaffolds. In terms of *in vivo* biosafety, we extracted the heart, liver, spleen, lung and kidney organs of experimental animals for tissue sections, and found no obvious abnormalities or residues of graphene derivatives (Fig. S4, ESI†). Taken together, compared with GelMA, rGO/GelMA has a stronger ability to promote the osteogenic differentiation of BMSCs, which is consistent with our previous *in vitro* results.

4. Conclusion

In conclusion, we fabricated rGO/GelMA scaffolds by applying 3D printing technology. The scaffolds with suitable pore sizes showed excellent biocompatibility and proliferation ability. The 0.05% rGO/GelMA scaffold has an excellent pore size of 26.35 ± 0.5 μm and good mechanical properties, which can promote the adhesion of BMSCs and SCs, and maintain high dryness and continuous proliferation within 7 days. *In vitro* experiments, alizarin red and alkaline phosphatase staining demonstrated its excellent osteogenic induction ability. In rats, 0.05% rGO/GelMA scaffolds loaded with both BMSCs and SCs achieved osteogenesis and neurogenesis 2 months after transplantation. This is attributed to the high adhesion capacity of the scaffold material and the potential for osteogenic/neural differentiation. Due to their flexibility as bioinks in 3D printing, GelMA hydrogels mixed with rGO are expected to have broad applications in multicellular delivery and functional tissue regeneration.

Author contributions

Xinwei Zhang: writing – original draft, conceptualization, methodology, data curation. Hao Zhang: visualization, editing. Yi

Zhang: data curation, investigation. Huimin Huangfu: data curation, investigation. Yixin Yang: software, validation. Qiuyue Qin: software. Yidi Zhang: conceptualization, methodology, formal analysis, project administration. Yanmin Zhou: conceptualization, project administration, supervision, funding acquisition.

Conflicts of interest

There are no conflicts to declare.

Acknowledgements

This study was supported by the National Natural Science Foundation of China (Grant No. 82071152), the Development and Reform Commission of Jilin Province (Grant No. 2021C042-1), and the Jilin Provincial Science and Technology Department (Grant No. 20200201302JC).

References

1 R. L. Meng Zhang, X. Wang, J. Xue, C. Deng, C. Feng, H. Zhuang, J. Ma, C. Qin, L. Wan, J. Chang and C. Wu, *Sci. Adv.*, 2020, **6**, eaaz6725.
2 M. Qu, C. Wang, X. Zhou, A. Libanori, X. Jiang, W. Xu, S. Zhu, Q. Chen, W. Sun and A. Khademhosseini, *Adv. Healthcare Mater.*, 2021, **10**, e2001986.
3 T. Y. L. Alessandra Marrella and D. H. Lee, *Mater. Today*, 2017, **10**, 1016.
4 F. X. Li, F. Xu, X. Lin, F. Wu, J. Y. Zhong, Y. Wang, B. Guo, M. H. Zheng, S. K. Shan and L. Q. Yuan, *Front. Endocrinol.*, 2020, **11**, 77.
5 S. Grässel, *Grässel Arthritis Res. Ther.*, 2014, **6**, 485.
6 M. A. Fernandez-Yague, S. A. Abbah, L. McNamara, D. I. Zeugolis, A. Pandit and M. J. Biggs, *Adv. Drug Delivery Rev.*, 2015, **84**, 1–29.
7 J. Cao, S. Zhang, A. Gupta, Z. Du, D. Lei, L. Wang and X. Wang, *Int. J. Med. Sci.*, 2019, **16**, 831–837.
8 R. E. Tomlinson, B. A. Christiansen, A. A. Giannone and D. C. Genetos, *Front. Endocrinol.*, 2020, **11**, 646.
9 C. Y. Yu and P. V. Abbott, *Aust. Dent. J.*, 2016, **61**, 39–58.
10 M. Zhang, C. Qin, Y. Wang, X. Hu, J. Ma, H. Zhuang, J. Xue, L. Wan, J. Chang, W. Zou and C. Wu, *Addit. Manuf.*, 2022, **54**, 102721.
11 X. Xue, Y. Hu, Y. Deng and J. Su, *Adv. Funct. Mater.*, 2021, **31**, 2009432.
12 C. C.-S. Claudio Bordignon and M. P. Colombo, *Haematologica*, 1999, **84**, 1110–1149.
13 L. S. Neves, M. T. Rodrigues, R. L. Reis and M. E. Gomes, *Expert Rev. Precis. Med. Drug Dev.*, 2016, **1**, 93–108.
14 H. Liu, Q. Zhang, S. Wang, W. Weng, Y. Jing and J. Su, *Bioact. Mater.*, 2022, **14**, 169–181.
15 Y. Han, X. Li, Y. Zhang, Y. Han, F. Chang and J. Ding, *Cells*, 2019, **8**, 886.
16 I. R. Avanzi, J. R. Parisi, A. Souza, M. A. Cruz, C. C. S. Martignago, D. A. Ribeiro, A. R. C. Braga and A. C. Renno, *J. Biomed. Mater. Res., Part B*, 2022, 1–17.
17 K. M. Wong, E. Babetto and B. Beirowski, *Neural Regener. Res.*, 2017, **12**, 518–524.
18 R. Li, D. Li, C. Wu, L. Ye, Y. Wu, Y. Yuan, S. Yang, L. Xie, Y. Mao, T. Jiang, Y. Li, J. Wang, H. Zhang, X. Li and J. Xiao, *Theranostics*, 2020, **10**, 1649–1677.
19 S. Shimizu, M. Kitada, H. Ishikawa, Y. Itokazu, S. Wakao and M. Dezawa, *Biochem. Biophys. Res. Commun.*, 2007, **359**, 915–920.
20 J. Wang, W. Zheng, L. Chen, T. Zhu, W. Shen, C. Fan, H. Wang and X. Mo, *ACS Biomater. Sci. Eng.*, 2019, **5**, 2444–2456.
21 K. Zhihui and D. Min, *ACS Biomater. Sci. Eng.*, 2022, **8**, 2849–2857.
22 C. Liao, Y. Li and S. C. Tjong, *Int. J. Mol. Sci.*, 2018, **19**, 3564.
23 X. P. Li, K. Y. Qu, B. Zhou, F. Zhang, Y. Y. Wang, O. D. Abodunrin, Z. Zhu and N. P. Huang, *Colloids Surf., B*, 2021, **205**, 111844.
24 K. Zhou, P. Yu, X. Shi, T. Ling, W. Zeng, A. Chen, W. Yang and Z. Zhou, *ACS Nano*, 2019, **13**, 9595–9606.
25 Z. Huang, M. Sun, Y. Li, Z. Guo and H. Li, *J. Mater. Chem. B*, 2021, **9**, 2656–2665.
26 S. R. Shin, C. Zihlmann, M. Akbari, P. Assawes, L. Cheung, K. Zhang, V. Manoharan, Y. S. Zhang, M. Yuksekkaya, K. T. Wan, M. Nikkhah, M. R. Dokmeci, X. S. Tang and A. Khademhosseini, *Small*, 2016, **12**, 3677–3689.
27 H. Li, C. Tan and L. Li, *Mater. Des.*, 2018, **159**, 20–38.
28 A. Schwab, R. Levato, M. D'Este, S. Piluso, D. Eglin and J. Malda, *Chem. Rev.*, 2020, **120**, 11028–11055.
29 Z. Chen, D. Zhao, B. Liu, G. Nian, X. Li, J. Yin, S. Qu and W. Yang, *Adv. Funct. Mater.*, 2019, **29**, 1900971.
30 N. Paxton, W. Smolan, T. Bock, F. Melchels, J. Groll and T. Jungst, *Biofabrication*, 2017, **9**, 044107.
31 X. Cui, J. Li, Y. Hartanto, M. Durham, J. Tang, H. Zhang, G. Hooper, K. Lim and T. Woodfield, *Adv. Healthcare Mater.*, 2020, **9**, e1901648.
32 C. K. Kuo and P. X. Ma, *J. Biomed. Mater. Res., Part A*, 2008, **84**, 899–907.
33 L. Dong, Z. Bu, Y. Xiong, H. Zhang, J. Fang, H. Hu, Z. Liu and X. Li, *Int. J. Biol. Macromol.*, 2021, **188**, 72–81.
34 X. Xue, Y. Hu, S. Wang, X. Chen, Y. Jiang and J. Su, *Bioact. Mater.*, 2022, **12**, 327–339.
35 X. Bai, M. Gao, S. Syed, J. Zhuang, X. Xu and X. Q. Zhang, *Bioact. Mater.*, 2018, **3**, 401–417.
36 A. Gutierrez-Fernandez, M. Inada, M. Balbin, A. Fueyo, A. S. Pitiot, A. Astudillo, K. Hirose, M. Hirata, S. D. Shapiro, A. Noel, Z. Werb, S. M. Krane, C. Lopez-Otin and X. S. Puente, *FASEB J.*, 2007, **21**, 2580–2591.
37 J. Liu, M. Qu, C. Wang, Y. Xue, H. Huang, Q. Chen, W. Sun, X. Zhou, G. Xu and X. Jiang, *Small*, 2022, **18**, e2106172.
38 M. D. Ranieri Cancedda, G. Bianchi, A. Derubeis and R. Quarto, *Stem Cells*, 2003, **21**, 610–619.
39 B. N. Kharbikar, P. Mohindra and T. A. Desai, *Cell Stem Cell*, 2022, **29**, 692–721.

40 J. Y. Ng, S. Obuobi, M. L. Chua, C. Zhang, S. Hong, Y. Kumar, R. Gokhale and P. L. R. Ee, *Carbohydr. Polym.*, 2020, **241**, 116345.
41 Y. Wang, Y. Xiao, G. Gao, J. Chen, R. Hou, Q. Wang, L. Liu and J. Fu, *J. Mater. Chem. B*, 2017, **5**, 511–516.
42 W. Guo, S. Wang, X. Yu, J. Qiu, J. Li, W. Tang, Z. Li, X. Mou, H. Liu and Z. Wang, *Nanoscale*, 2016, **8**, 1897–1904.
43 S. E. D'Souza, *Elsevier Science Publisher*, 1991, **91**, pp. 0376–5067.
44 Y. Dong, P. Li, C.-B. Chen, Z.-H. Wang, P. Ma and G.-Q. Chen, *Biomaterials*, 2010, **31**, 8921–8930.
45 J. Yan, R. Wu, S. Liao, M. Jiang and Y. Qian, *Front. Bioeng. Biotechnol.*, 2020, **8**, 590998.
46 L. Zhang, L. Xu, G. Li and Y. Yang, *Colloids Surf., B*, 2019, **173**, 689–697.
47 Y. Qian, X. Zhao, Q. Han, W. Chen, H. Li and W. Yuan, *Nat. Commun.*, 2018, **9**, 323.
48 S. Hosseinpour, L. J. Walsh and C. Xu, *J. Mater. Chem. B*, 2020, **8**, 9863–9876.
49 X. Ye, Z. He, Y. Liu, X. Liu, R. He, G. Deng, Z. Peng, J. Liu, Z. Luo, X. He, X. Wang, J. Wu, X. Huang, J. Zhang and C. Wang, *Int. J. Mol. Sci.*, 2022, **23**, 9722.
50 Y. Zhang, T. Lin, H. Meng, X. Wang, H. Peng, G. Liu, S. Wei, Q. Lu, Y. Wang, A. Wang, W. Xu, H. Shao and J. Peng, *J. Orthop. Transl.*, 2022, **33**, 13–23.
51 D. Gan, Y. Jiang, Y. Hu, X. Wang, Q. Wang, K. Wang, C. Xie, L. Han and X. Lu, *J. Orthop. Transl.*, 2022, **33**, 120–131.
52 A. Raslan, L. Saenz Del Burgo, J. Ciriza and J. L. Pedraz, *Int. J. Pharm.*, 2020, **580**, 119226.
53 J. An, H. Yang, Q. Zhang, C. Liu, J. Zhao, L. Zhang and B. Chen, *Life Sci.*, 2016, **147**, 46–58.
54 W. C. Lee, C. H. Y. X. Lim, H. Shi, L. A. L. Tang, Y. Wang, C. T. Lim and K. P. Loh, *ACS Nano*, 2022, **5**, 7334–7341.
55 P. B. A. Scutt and M. Brautigam, *Calcif. Tissue Int.*, 1996, **59**, 154–162.
56 D. Mohammadrezaei, H. Golzar, M. Rezai Rad, M. Omidi, H. Rashedi, F. Yazdian, A. Khojasteh and L. Tayebi, *J. Biomed. Mater. Res., Part A*, 2018, **106**, 2284–2343.
57 J. A. Pereira, F. Lebrun-Julien and U. Suter, *Trends Neurosci.*, 2012, **35**, 123–134.
58 G. Nocera and C. Jacob, *Cell. Mol. Life Sci.*, 2020, **77**, 3977–3989.
59 Q. Zhao, M. Shi, C. Yin, Z. Zhao, J. Zhang, J. Wang, K. Shen, L. Zhang, H. Tang, Y. Xiao and Y. Zhang, *Nano-Micro Lett.*, 2020, **13**, 28.
60 Y. Liu, D. Luo and T. Wang, *Small*, 2016, **12**, 4611–4632.
61 R. J. Miron and Y. F. Zhang, *J. Dent. Res.*, 2012, 736–744.
62 S. Mukherjee, P. Sriram, A. K. Barui, S. K. Nethi, V. Veeriah, S. Chatterjee, K. I. Suresh and C. R. Patra, *Adv. Healthcare Mater.*, 2015, 1722–1732.
63 X. Yao, Z. Yan, X. Wang, H. Jiang, Y. Qian and C. Fan, *Regener. Biomater.*, 2021, 1–9.